Supporting Information

Preparations: Doxoves® and Doxorubicin. Doxoves®, or DOX®, (F30204B-D) was purchased from FormuMax Scientific (Sunnyvale, CA, USA). DOX® liposomes are dissolved in the manufacturer's buffer containing 10 mM Histidine and 10% sucrose at pH=6,5. DOX® was stored at 4ºC. Two different batches of DOX® were measured and included, separately (see Fig. S4), in this work. The majority of measurements were performed on DOX® from Batch#1, which are included in the main text. Measurements on DOX® from Batch#2 were performed primarily to confirm data from Batch#1. Doxorubicin hydrochloride (powder) was purchased from Sigma Aldrich (Milan, Italy) and dissolved in water at a concentration of 2 mg/ml, then stored at -20ºC.

Preparations: ribbon-shaped Doxorubicin crystals. To prepare DOX crystals, a solution of Doxorubicin HCl (10 mg/mL) was added dropwise into a 2-mL solution of ammonium sulfate (pH=5.5) with a concentration of 500 mM, under magnetic stirring (please note: when the solution turns turbid the titration endpoint is reached and a precipitate is formed). The precipitate was poured out into a WillCo plate to rest until it was completely dry.

Preparations: Doxorubicin-loaded liposomes. Hydrogenated soybean phosphatidylcholine (HSPC), cholesterol, and DSPE-PEG2k were obtained from Avanti Polar Lipids (Alabaster, AL, USA). Doxorubicin-loaded liposomes were prepared by the thin lipid film method. In brief, HSPC, cholesterol and DSPE-PEG2k (56.3:38.4:5.3 mol%) were dissolved in chloroform and the organic solvent was evaporated by rotary evaporation under reduced pressure at room temperature for 2-hours. Multilamellar vesicles (MLVs) were formed by hydrating the lipid film for 3h at 50°C with 250 mM ammonium sulphate AS (final lipid concentration, 1.5 mg/ml). Doxorubicin hydrochloride was dissolved in 250 mM AS (pH = 7.4) (drug concentration 0,15 mg/ml, i.e., 260 mM). Doxorubicin-loaded SUVs were prepared by adding doxorubicin hydrochloride solution to SUVs. Subsequently, unloaded Doxorubicin was removed by dialysis for 30 min at 8900 rpm. At the end, Doxorubicin-loaded liposomes (also referred to as DOX®-like nanoparticles, or DLNs) were of 1 mg/mL total lipids and 0.05 mg/mL total Doxorubicin (i.e. 86 mM). The doxorubicin to lipid weight ratio used in the remote loading was maintained at 0.05. As final step, the buffer containing DLNs was brought to 10 mM Histidine and 10% sucrose at pH=6,5 and stored at 4ºC.

Preparations: mechanical destruction of liposomes by spin coater. To destroy mechanically DOX® and DLN, samples were seeded on a glass Petri dish and then spin-coated for 1 min at 5000 rpm. The aqueous solution is naturally lost during the procedure. Doxorubicin crystals and/or membrane patches adhere directly on the glass.

Atomic Force Microscopy. Topographic measurements were performed employing a commercial Dimension Icon AFM (Bruker) operating in PeakForce Tapping™ (PFT) mode and using ScanAsyst™-air probes (nominal elastic constant 0.4 N m−1). PFT-mode imaging is performed by nano-indenting the sample pixel-by-pixel controlling the force applied by the tip with high accuracy.

Fluorescence Lifetime Imaging experiments, phasor analysis, and phasor rules of composition.

Before each FLIM measurement, a drop of approximately 50 µl of DOX® (or DLN) stock solution was poured on the glass of a WillCo plate, without any further dilution. For what concerns the free drug, the 2 mg/ml DOX stock solution was diluted in water prior to FLIM at a final concentration of ~2 µg/ml. For what concerns DOX crystals and spin-coated liposomes, they were obtained as dry samples directly on the glass of a WillCo plate, as described above. No aqueous solution was added prior to FLIM to avoid any possible drug re-suspension.

FLIM was performed by using Leica TCS SP5 confocal microscope (Leica Microsystems, Mannheim, Germany). The samples were observed by a pulsed diode laser operating at 40 MHz with an excitation wavelength of 470 nm (the average power at the sample was 10-20 μW). The emission was collected in the wavelength range between 520 and 650 nm by a photomultiplier tube interfaced with a time correlated single photon counting (TCSPC) card (PicoHarp 300, PicoQuant, Berlin).

The phasor analysis of experimental lifetime acquisitions was performed by using a dedicated routine of SimFCS software (Laboratory for Fluorescence Dynamics, University of California, Irvine). Technically: for each pixel in the image, the fluorescence decays measured in time-domain are mapped onto the so-called "phasor" plot, where a phasor has two coordinates: the real and imaginary parts of the Fourier transform of the fluorescence lifetime decay (with area under the curve normalized at 1), calculated at the angular repetition frequency of the measurement ('*w*' in Eq. S2-S3). The phasors stay within the half-disk centered at (½,0) with radius ½ and positive *x*, where the zero lifetime is located at (1,0) and the infinite lifetime at (0,0). This suggests that by taking the Fourier transformation of a measured decay curve, the lifetime can be estimated based on the position of the phasor inside this so-called universal (semi)circle. The distribution of phasor points originating from FLIM measurements appears on the universal circle for mono-exponential decays, or inside the circle for multi-exponential decays.

In this work, most of the measured decays are described by the sum of three exponentials, each corresponding to a specific supramolecular organization of DOX. The intensity can be then expressed as:

$$I(t) = A_f e^{-t/\tau_f} + A_b e^{-t/\tau_b} + A_c e^{-t/\tau_c} \qquad \text{Eq. S1}$$

where:

- 'f', 'b' and 'c' subscripts indicate DOX in the free, membrane-associated and crystallized forms, respectively
- A_i are the amplitudes of the exponential components
- τ_i are the characteristic lifetimes of the species

The calculated phasor coordinates ('*g*' and '*s*') from this decay are given by:

$$g(w) = \left(A_f\tau_f \frac{1}{1+(w\tau_f)^2} + A_b\tau_b \frac{1}{1+(w\tau_b)^2} + A_c\tau_c \frac{1}{1+(w\tau_c)^2} \right) / \left(A_f\tau_f + A_b\tau_b + A_c\tau_c \right) \qquad \text{Eq. S2}$$

$$s(w) = \left(A_f\tau_f \frac{w\tau_f}{1+(w\tau_f)^2} + A_b\tau_b \frac{w\tau_b}{1+(w\tau_b)^2} + A_c\tau_c \frac{w\tau_c}{1+(w\tau_c)^2} \right) / \left(A_f\tau_f + A_b\tau_b + A_c\tau_c \right) \qquad \text{Eq. S3}$$

where:

- w is the angular repetition frequency of the laser modulation.

These expressions can be simplified using the general definition of 'fractional intensity' of a species 'n' (F_n), already presented in previous reports (Refs. S1-S2):

$$F_n = A_n\tau_n / \sum_n A_n\tau_n \qquad \text{Eq. S4}$$

The phasor coordinates modified according to Eq. S4 are thus are given by:

$$g(w) = F_f \frac{1}{1 + (w\tau_f)^2} + F_b \frac{1}{1 + (w\tau_b)^2} + F_c \frac{1}{1 + (w\tau_c)^2} \qquad \text{Eq. S5}$$

$$s(w) = F_f \frac{w\tau_f}{1 + (w\tau_f)^2} + F_b \frac{w\tau_b}{1 + (w\tau_b)^2} + F_c \frac{w\tau_c}{1 + (w\tau_c)^2} \qquad \text{Eq. S6}$$

With: $F_f + F_b + F_c = 1$

The final result (Eqs. S5 and S6) is the law of phasor addition (which can be generalized to any number of monoexponential decaying species, and originally presented by Gregorio Weber, Ref. S3), which helps in identifying the origin of points in the phasor plot. If two molecular species are coexisting in the same pixel, for instance, all the possible weighting combinations of the two molecular species give phasors distributed along a straight line joining the characteristic phasors of the two pure species. In the case of three molecular species, the possible realizations of the system fill a triangle where the vertices correspond again to the characteristic phasors of the pure species. Thus, given an experimental phasor that is the combination of two (or more) species, and the phasors of the isolated pure components, a graphical solution can be derived as described previously by others (Ref. S1) and schematically shown in Fig. S1. In brief: a line connecting each characteristic phasor from pure species with the composite experimental phasor (black dot in Fig. S1) is drawn and extended to the line joining the remaining two pure-species characteristic phasors. Then, the calculation of the fractional-intensity contribution of each pure species "*i*" is performed using the following relation:

$$F_i = \frac{distance_{point \rightarrow intercept}}{distance_{i \rightarrow intercept}} \qquad \text{Eq. S7}$$

Where "point" refers to the position of the experimental phasor of the composite sample (black dot in Fig. S1). This can be alternatively conceived as follows: if we assume that there are only two pure components initially (with characteristic lifetime labelled by the 'green' and the 'blue' dots in Fig. S1 for instance) contributing to the position of the experimental phasor of the composite sample, then this latter would lie along the line joining the characteristic phasors of the two pure species. At this point, the larger the contribution of a third species eventually added to the system (with characteristic lifetime labelled by 'red' dot in Fig. S1, for instance), the closer the experimental phasor of the composite sample will be to the 'red' reference vertex.

Absorption and Fluorescence spectroscopy. Absorption spectra in the UV-Visible spectral range were measured using a spectrophotometer (mod. Lambda 950, Perkin Elmer) equipped with holders for both solid-state samples and solutions. The contribution of optical scattering to the measured spectra was evaluated by fitting the data of the long-wavelength range of the measured spectra (>700 nm) and of the interval 330-350 nm to a λ^{-b} function, as reported in the Refs. S4-S5. The typical values of parameter *b* resulting from the fitting procedure are in the range 1.9-2.1, which are in line with the results of Ref. S6. The resulting scattering background is subtracted from the measured absorption spectra. In addition, absorption spectra were measured by using an integration sphere (Labsphere), following the methodology reported in Ref. S7 for the measurement of the absorption. To this aim, samples were illuminated by a calibrated broadband lamp (Ref. S8) and the spectra of the optical signals collected from the integration sphere were measured by a fiber-coupled monochromator (mod. Flame, Ocean Optics). The fraction of light intensity absorbed by the samples and the photoluminescence quantum yield of the DOX_f and of the DOX_c samples were also measured by using the integration sphere and the methodology of Ref. S8.

Briefly, the samples were optically pumped by a diode laser at 488 nm (mod. L6Cc, Oxxius), whereas a light-emitting diode (LED) with emission peaked at 470 was used for evaluating the absorption at this wavelength. The intensities of the excitation laser and of the fluorescence emitted by the samples were measured by the fiber-coupled monochromator. Such measurements were performed in different configurations as described in Ref. S8, namely with the excitation laser hitting the internal surface of the sphere and without sample inside the sphere (a configuration hereafter denoted by the superscript "SL"), and with the sample placed in the sphere both along the laser path (a configuration hereafter denoted by the superscript "LonS") and out of the laser path (a configuration hereafter denoted by the superscript "LoutS"). The measured intensities of the laser and of the photoluminescence were corrected for the spectral response of the whole detection system, which accounts for the reflectance of the coating of the integration sphere, the attenuation of the optical fiber and the overall detection efficiency of the spectrometer, and for the contribution of the cuvette and substrate, and they were divided by their respective integration times. The fraction of light absorbed by the samples (A_s) and the photoluminescence quantum yield (QY_{PL}) are calculated as:

$$A_s = 1 - \frac{I_L^{LonS}}{I_L^{LoutS}} \qquad \text{Eq. S8}$$

$$QY_{PL} == \frac{I_{PL}^{LonS} - (1 - A_s) I_{PL}^{LoutS}}{I_L^{SL} A_s} \qquad \text{Eq. S9}$$

where I_L and I_{PL} are the corrected intensities of the laser and of the photoluminescence, respectively, in the various measurement configurations.

Concerning the experiment on DLN and DOX® in solution, absorption and fluorescence spectra were recorded in cuvette with 1-cm optical path (Hellma, Müllheim, Germany) at 23ºC on a JASCO V550 spectrophotometer (JASCO, Easton, MD, USA) and a Cary Eclipse spectrofluorometer (Varian, Palo Alto, CA, USA), respectively. Before absorbance/fluorescence measurements, stock solutions of DLN and DOX®were diluted in a water solution with addition of 10 mM Histidine, 10% sucrose, and pH=6,5 to reproduce the manufacturer's buffer conditions.. Free DOX, used as a reference material, was dissolved in water. Fluorescence spectra were obtained with excitation wavelength of 470 nm, and fluorescence emission was integrated between 500 and 700 nm. UV-VIS spectra were corrected for scattering by using a linear fit in the ranges 350±10, 580±10. Absorbance(470nm) vs fluorescence plots were fitted with linear regression. The ratio between the slope of DLN (or DOX®) and that of DOX was used to derive the ratio between the QYs. The absolute QY_{PL} of DLN (or DOX®) was then calculated by using the independently measured QY of DOX (i.e. 4.23±0.09, Tab. 1).

Quantum yields and extinction coefficients: uncertainty propagation and conversion of fractional intensity contributions to molar fractions. The quantum yield of DOX_f and DOX_c was calculated as described above. The one of DOX_b was derived by the one of DOX_f multiplied by the ratio of their lifetimes (as explained in the main text). The uncertainty on quantum yields QY_i was considered to be the standard error on n_i independent measurements (n_c=6, n_f=3), except for QY_b where it has been calculated by standard propagation of independent uncertainties, and has been considered uncorrelated with the other uncertainties.

The extinction coefficient ε_f for the free form DOX_f has been derived from the corresponding A_s, by means of the Lambert-Beer relation for a homogeneous optical path length of 1 cm; the uncertainty is the standard error on 3 independent measurements. We estimated the extinction coefficient ε_b for the membrane form DOX_b to have value and uncertainty as the free form, but the uncertainty has been considered uncorrelated.

The extinction coefficient ε_c of the crystal form DOX_c has been calculated starting from the corresponding A_s (see previous section). Confocal and AFM measurements on the deposited DOX_c showed that the thickness of the crystal layer was not homogeneous; therefore, we considered the Lambert-Beer law on a sample with non-homogeneous path length in the illuminated area:

$$T = \frac{\iint_S I_0(x,y) 10^{-\varepsilon_c c l(x,y)} dxdy}{\iint_S I_0(x,y) dxdy} = \frac{\iint_S 10^{-\varepsilon_c c l(x,y)} dxdy}{S}, \quad \text{(S10)}$$

where $T = 1 - A_s$ is the average transmittance of the area S, c=2.52 M is the concentration of DOX in the crystal calculated based on available crystallographic data (Ref. S9), $l(x,y)$ is the thickness of the crystal deposited on the glass at the point (x,y), $I_0(x,y)$ is the intensity of the incoming light at the point (x,y) within the illuminated area S, and for the last equivalence we considered a constant intensity I_0 within S. Having sampled $l(x,y)$ at various points p using AFM, (S10) becomes:

$$T = \frac{\sum_p 10^{-\varepsilon_c c l_p}}{n_p}, \quad \text{(S11)}$$

where l_p is the height of the crystal at pixel p and n_p is the total number of the considered pixel. In the AFM measurements we used the same sample used in the integrating sphere. The AFM images presented a trend and sometimes some "steps" (discontinuities in the heights) along the secondary scanned axis (*y*). For detrending, we used two strategies. In the first one (1 sample), where the sample was scanned as it was, the average along *x* for every row *y* was calculated, a smoothing was performed in any section where no clear discontinuities were present (Savitzy-Golay with a window of 51 points and polynomial order 3), the result was subtracted from all the pixels with the same *y*, and a constant was added to have the minimum height at 0. In a second series of experiments on the same sample, a scratch was done (more or less in the *y* direction), the average measured height was obtained at a given *y* from zones within the scratch where no residues were present, and this value was subtracted for all the pixel with such *y*. In this second case, the sum in (S11) was considered on pixels outside of the scratch, where there were clearly no additional residues which could have been deposited upon scratching the sample.

The transmittance T has been measured in n_T=3 independent measurements on the same sample as described above. We solved equation (S11) for ε_c (using the Symbolic Math Toolbox in MatLab, MathWorks©) for the three obtained values of T and for the three AFM images, calculated the averages

ε_c^T and standard errors $\sigma_{\bar{\varepsilon},T}$ on the three AFM measures for the three T measures, and made a weighted average of the three results:

$$\varepsilon_c = \sum_T \frac{\varepsilon_c^T}{\sigma_{\bar{\varepsilon},T}^2} \Big/ \sum_T \frac{1}{\sigma_{\bar{\varepsilon},T}^2}, \tag{S12}$$

with final uncertainty given by the square root of:

$$\sigma_{\bar{\varepsilon}_c}^2 = \frac{1}{\sum_T \frac{1}{\sigma_{\bar{\varepsilon},T}^2}} + \frac{\sum_T \left(\varepsilon_c^T - \varepsilon_c\right)^2}{(n_T - 1)n_T}. \tag{S13}$$

Inverting the order of the operations, the results for average ε_c and $\sigma_{\bar{\varepsilon}_c}$ where almost identical (7510±490 $M^{-1}cm^{-1}$ averaging first on AFM measures and then on the T values, versus 7500±480 $M^{-1}cm^{-1}$ performing the operations in the opposite order). The three brightnesses $\alpha_i = QY_i * \varepsilon_i$ were then calculated, with uncertainties $\sigma_{\bar{\alpha}_i}$ obtained by standard propagation of independent uncertainties. The fractional-intensity contributions $F_{i,f}$ for the three species have been measured in n_f=24 independent experiments. F_i is the average over f of the $F_{i,f}$, and the covariance matrix amongst these values has been calculated as:

$$\sigma_{F_i F_j} = \frac{\sum_f \left(F_{i,f} - F_i\right)\left(F_{j,f} - F_j\right)}{n_f - 1}. \tag{S14}$$

The molar fractions can be calculated as:

$$F_i^{corr} = \frac{F_i}{\alpha_i} \Big/ \sum_j \frac{F_j}{\alpha_j}; \tag{S15}$$

and the uncertainties can be calculated from:

$$\sigma_{F_i^{corr}}^2 = \sum_{\gamma,\delta} \frac{\partial F_i^{corr}}{\partial \gamma} \frac{\partial F_j^{corr}}{\partial \delta} \sigma_{\gamma\delta} = \sum_i \left(\left| \frac{\partial F_i^{corr}}{\partial \alpha_i} \right|^2 \sigma_{\bar{\alpha}_i}^2 + \left| \frac{\partial F_i^{corr}}{\partial F_i} \right|^2 \sigma_{F_i}^2 \right) + \sum_{i>j} 2 \frac{\partial F_i^{corr}}{\partial F_i} \frac{\partial F_j^{corr}}{\partial F_i} \sigma_{ij} \tag{S16}$$

with γ,δ in $(\{\alpha_i\},\{F_i\})$ and, in general, $\sigma_\gamma^2 = \sigma_{\gamma\gamma}$ and $\sigma_{\gamma\delta} = 0$ for uncorrelated entities.

Note that, for two species only, the sum of the two fractions must be 1, so the two fractions are perfectly anticorrelated (the two variances are the same and the covariance is equal to the opposite of the variance), so it is better to use the equation:

$$F_i^{corr} = \frac{F_i}{\alpha_i} \Big/ \left(\frac{F_i}{\alpha_i} + \frac{1 - F_i}{\alpha_j} \right) = \left[1 + \frac{\alpha_i}{\alpha_j} \left(\frac{1}{F_i} - 1 \right) \right]^{-1} \quad (i \neq j), \tag{S17}$$

and the equation (S16) with the three uncorrelated variables F_i, α_i, α_j.

In all cases, we calculated the uncertainties on the final quantities as expected from single measurements, equivalents to the standard deviation for a population. Therefore, we used the standard deviation for the F_i, but the statistical uncertainty on the "true" values of the parameters α_i (equivalent to the standard error). It is important to note that the displayed uncertainties reflect only the statistical ones in our experiments. Systematic errors might arise from the used approximations. E.g., we considered the interaction of light with the fluorophore to be the same for DOX_b and DOX_f, considering only a weaker non-radiative decay for the membrane form. Moreover, we could not check if the crystal deposited on glass, organized in a web of stripes with nanometric dimensions, has a density different from the one of a bulk crystal; or if these nanometric features have a more complicated effect on the light wave (due to refraction and diffraction) than the one expected from an "average" application of the Lambert-Beer law.

The quantum yield QY_{mix} of a mix of different species is given by:

$$QY_{mix} = \frac{\sum_i \varepsilon_c F_i^{corr} QY_i}{\sum_i \varepsilon_c F_i^{corr}} = \frac{\sum_i F_i}{\sum_i F_i / QY_i} = \left(\sum_i \frac{F_i}{QY_i} \right)^{-1}, \tag{S18}$$

and its uncertainty can be calculated with an equation similar to (S16).

A final round of data analysis builds on an independent experiment performed using KI as quencher of DOX (purchased from Sigma Aldrich, Milan, Italy), with the specific goal of identifying DOX molecules exposed to the medium in which KI is dissolved. In brief, we extracted the fraction of DOX_f and DOX_b affected by KI at 370 mM as compared to a control experiment in absence of KI. This calculation is made by assuming that the DOX_c species, buried within the lipid nanoparticle, cannot be affected by KI (which is membrane impermeable). Thus, the measured fractions of either DOX_f or DOX_b in presence of KI ($F_i^{post\ KI}$) were corrected considering the apparent slight variation detected in the fractional-intensity contribution of DOX_c according to:

$$F_i^{post\ KI - corr} = F_i^{post\ KI} * \frac{F_c^{pre\ KI}}{F_c^{post\ KI}} \qquad \text{Eq. S19}$$

Then, the percentage of either DOX_f or DOX_b buried inside the lipid nanoparticle (or, conversely, exposed to the medium) are easily derived, according to:

$$\%F_i^{int} = \frac{F_i^{post\ KI - corr}}{F_i^{pre\ KI}} \times 100 \qquad \text{Eq. S20}$$

From the experiments with KI used as a quencher: after addition of KI, 65.1 ± 4.3% of the free form is switched off; 37.9 ± 6.9% of the membrane-bound form is switched off (Tab. S1).

Supplementary References

[S1] S. Ranjit, R. Datta, A. Dvornikov, E. Gratton. Multicomponent Analysis of Phasor Plot in a Single Pixel to Calculate Changes of Metabolic Trajectory in Biological Systems. *J. Phys. Chem.* A **2019**, *123*, 9865

[S2] A. Vallmitjana, A. Dvornikov, B. Torrado, D.M. Jameson, S. Ranjit, E. Gratton. Resolution of 4 components in the same pixel in FLIM images using the phasor approach. *Methods Appl. Fluoresc.* **2020**, *8*, 035001

[S3] G. Weber. Resolution of the fluorescence lifetimes in a heterogeneous system by phase and modulation measurements. *J. Phys. Chem.* **1981**, *85*, 949

[S4] J. N. Coleman, M. Lotya, A. O'Neill, S. D. Bergin, P. J. King, U. Khan, K. Young, A. Gaucher, S. De, R. J. Smith, I. V. Shvets, S. K. Arora, G. Stanton, H.-Y. Kim, K. Lee, G. T. Kim, G. S. Duesberg, T. Hallam, J. J. Boland, J. J. Wang, J. F. Donegan, J. C. Grunlan, G. Moriarty, A. Shmeliov, R. J. Nicholls, J. M. Perkins, E. M. Grieveson, K. Theuwissen, D. W. McComb, P. D. Nellist, V. Nicolosi. Two-Dimensional Nanosheets Produced by Liquid Exfoliation of Layered Materials. *Science* **2011**, *331*, 568

[S5] K. Wang, J. Wang, J. Fan, M. Lotya, A. O'Neill, D. Fox, Y. Feng, X. Zhang, B. Jiang, Q. Zhao, H. Zhang, J. N. Coleman, L. Zhang, W. J. Blau. Ultrafast Saturable Absorption of Two-Dimensional MoS_2 Nanosheets. *ACS Nano* **2013**, *7*, 9260.

[S6] G. S. He, H.-Y. Qin, Q. Zhen. Rayleigh, Mie, and Tyndall scatterings of polystyrene microspheres in water: Wavelength, size, and angle dependences. *J. Appl. Phys.* **2009**, 105, 023110.

[S7] J. C. de Mello, H. F. Wittmann, R. H. Friend. An Improved Experimental Determination of External Photoluminescence Quantum Efficiency. *Adv. Mater.* **1997**, *9*, 230.

[S8] R. Stair, W. E. Schneider, J. K. Jackson. A new Standard of Spectral Irradiance. *Appl. Opt.* **1963**, *2*, 1151.

[S9] L. Mathivathanan, G. Yang, F. Leng, R. G. Raptis. Crystal structure and conformational analysis of doxorubicin nitrate. *Acta Cryst.* **2018**, E74, 400.

Table S1. Results from FLIM experiments conducted before and after exposure of DOX® to KI.

	DOX®$_{FLIM}$ (pre-KI) †	**DOX®$_{FLIM}$ (post-KI)** ‡	**DOX® (%Ex/In)** ‖	
N	3	3	-	
DOX_f (%)	22.1±1.0	11.2±0.34	**Ex%**	65.1±4.3
			In%	34.9±4.3
DOX_b (%)	44.4±2.5	40.1±2.5	**Ex%**	37.9±6.9
			In%	62.1±6.9
DOX_c (%)	33.5±3.4	48.7±2.2	**In%**	100

† Results from N=3 experiments conducted on DOX® in absence of KI (reported as Mean±SD); ‡ Results from N=3 experiments conducted on DOX® in presence of 370 mM KI (reported as Mean±SD); ‖ The percentages of external ('Ex') and internal ('In') DOX_f and DOX_b reported here were calculated as described in SI (Eqs. S19-S20) assuming that DOX_c, being buried within the liposome, is not affected by the membrane-impermeable KI (values are Mean±SD).

Supplementary Figures

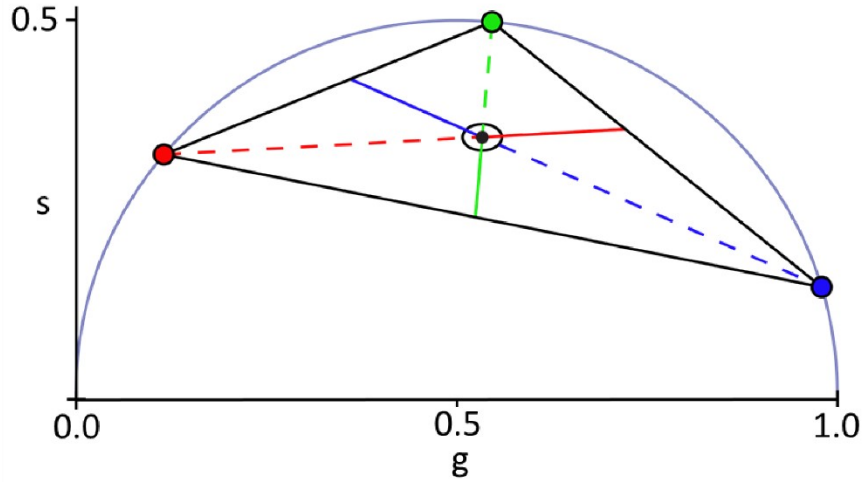

Fig. S1. Three-component analysis using phasor approach. The lines joining the characteristic phasors of pure species (red, blue and green, at the vertices of the triangle) and the phasor of the composite sample whose fractional intensity contributions are being calculated (the black point indicates the centroid of an experimentally derived cluster) are drawn and extended to the opposite side of the triangle (i.e. to the line joining the remaining two pure-species phasors). The distance of the black point and of each vertex from the opposite line (solid portion of each line and complete solid + dashed line, respectively) are used for the calculation of fractional intensity contribution, according to Eq. S7.

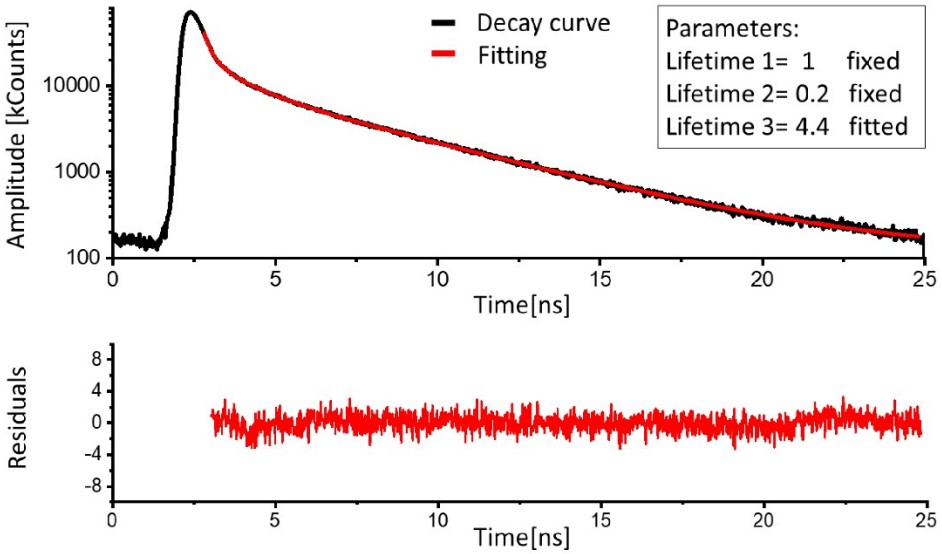

Fig. S2. Data fitting in the time domain suggests that the hypothetical third species should be characterized by a lifetime higher than ~4 ns, in keeping with expectations based on the phasor plot (dashed lines in Fig. 1). Top panel: typical lifetime decay curve of Doxoves® (black) with multiexponential fitting with three components (red). Bottom panel: fitting residues.

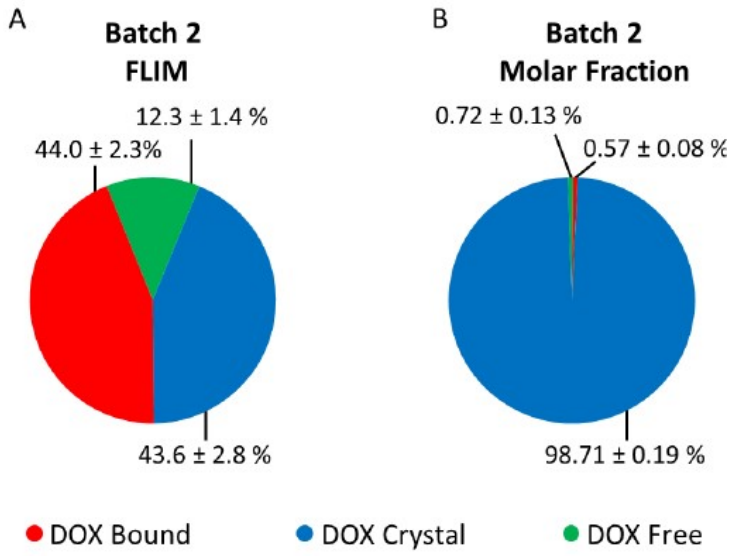

Fig. S3. Fractional intensity contribution (A) and molar fractions (B) of DOX_f, DOX_b, and DOX_c in a second batch of Doxoves®.

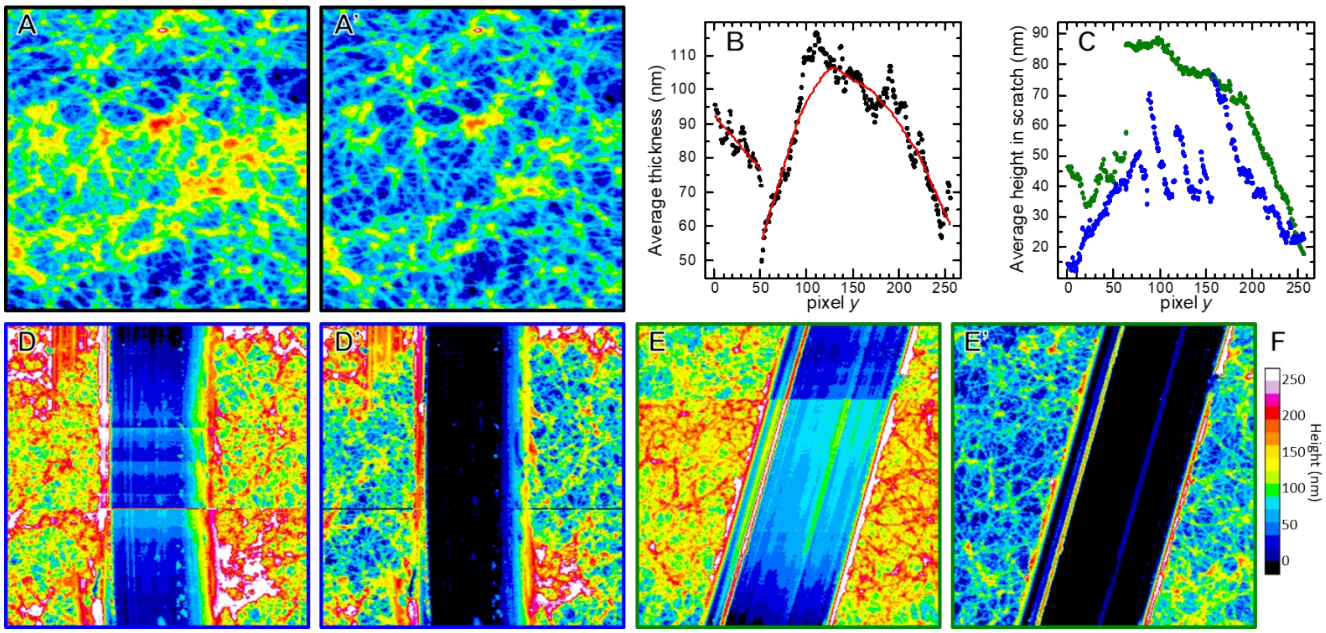

Fig. S4*:* AFM images of DOX_c deposited on a glass, and their detrending. A-A') AFM image of the sample before and after applying the slope line-by-line correction along the *y axis*. Images are of square areas of 20 µm side B) Black dots: average along *x* as a function of *y* for the image in panel A. Red curves: smoothing of the data in two different regions, used for correcting the image in A. C) Blue and green dots: average along *x* (as a function of *y*) of the heights measured by AFM inside the scratch visible in the AFM images of the scratched sample reported in panels D and E, respectively. These values were subtracted from all the pixels with corresponding *y* in the figures in panels D and E in order to obtain the images in panels D' and E', respectively. F) Common color scale for the heights represented in the images in panels A, A' and D-E'); all images in D-E' are of square areas of 40 µm side.

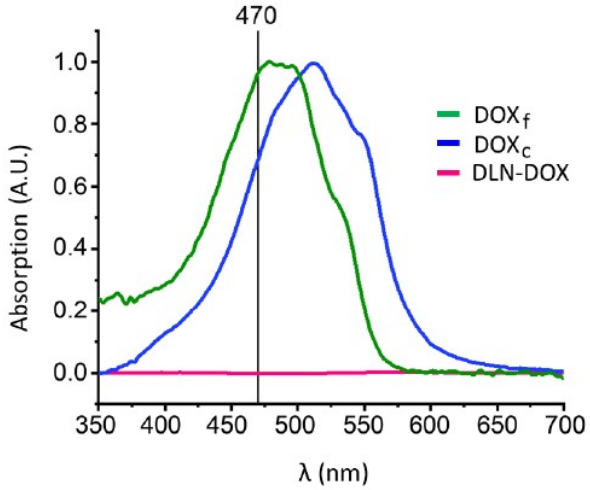

Fig. S5 Absorption spectra of DOX_f (green line) and DOX_c (blue line) as measured with the integration sphere. Spectra were normalized to 1 (A.U.). Absorption spectra of DLN and DOX_f (measured as described in Suppl. Materials and Methods and normalized to 1) were superimposable, as demonstrated by their difference (magenta line) being almost zero.

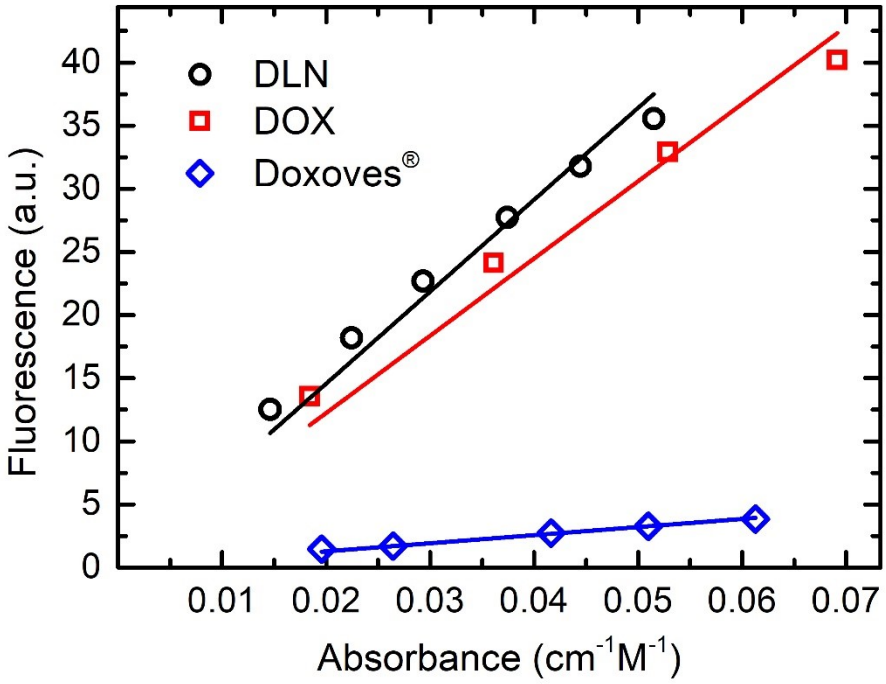

Fig. S6. Black dots, red squares, and blue diamonds: area under the peak of fluorescence emission versus absorbance at 470nm (after removal of the background estimated with a linear fit in the ranges 350±10, 580±10) for DLN (black dots), DOX (red squares), and DOX® (blue diamonds) at different concentrations. Lines of corresponding colors are linear fits with intercept fixed at 0. Ratios between the slopes correspond to ratio between QYs, and we used Doxorubicin as reference material. Absolute QYs were calculated by using the QY value for DOX experimentally determined here (4.23±0.09%). The resulting QYs are 5.03±0.25% for DLN and 0.45±0.02% for DOX®.

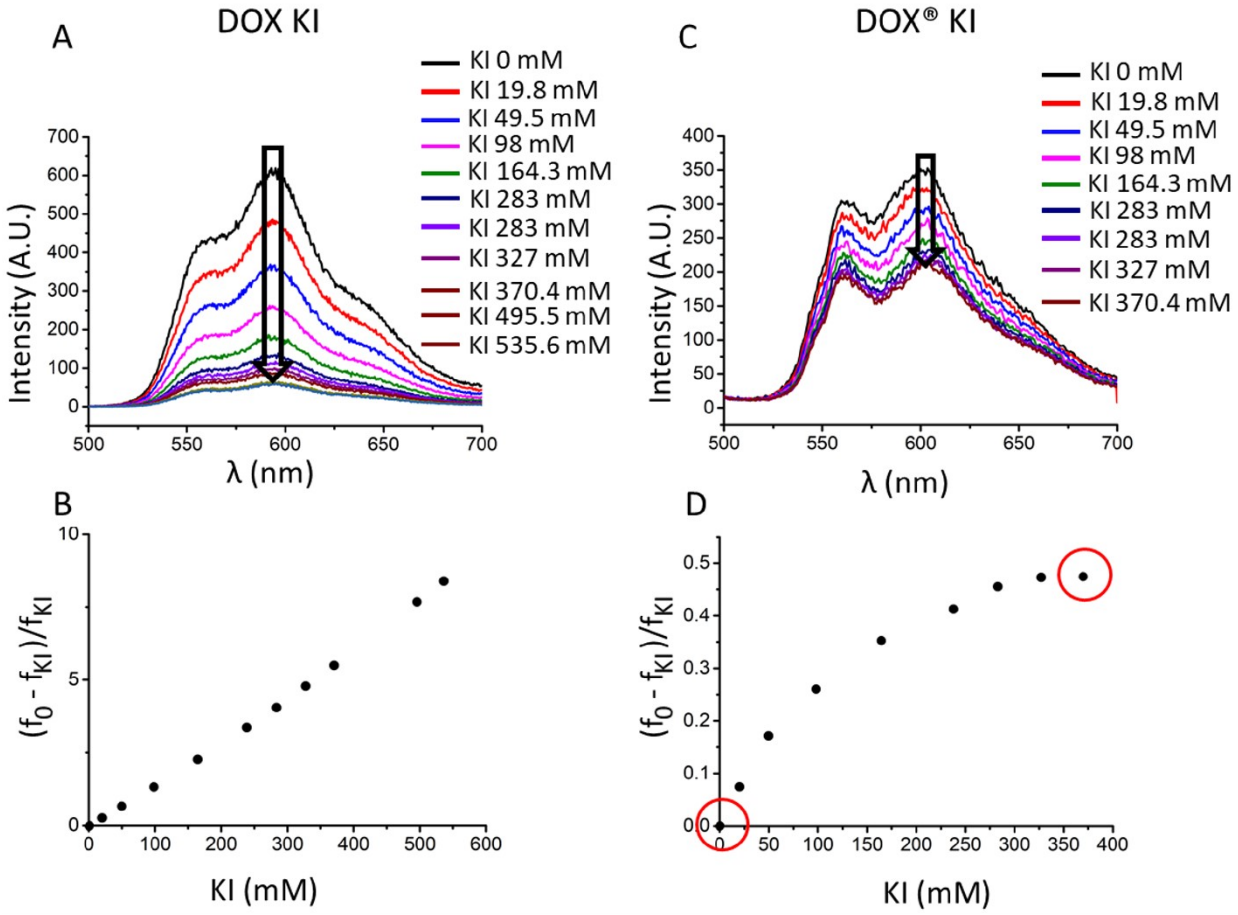

Fig. S7 (A) Effect of KI administered at different concentrations on DOX fluorescence emission, excited at 470 nm: KI proves to be an effective quencher of DOX molecules in solution. (B) $(f_0-f_{KI})/f_0$, where f_0 (f_{KI}) is the fluorescence intensity at 600 nm excited at 470 nm of a DOX_f sample without (with) KI, plotted as a function of KI concentration. (C-D) Same as in (A-B) but using DOX®. In this case, KI is able to quench only a fraction of DOX molecules (i.e. the plot in 'D' reaches a plateau at high KI concentrations). The two experimental conditions highlighted by the empty red circles (no KI and 370 mM KI) were also measured by FLIM (results reported in Tab. S1).